



HAL
open science

Tailoring the crystallographic texture of pure copper through control of the scanning strategy in Electron Powder Bed Fusion

Alizée Thomas, Guillaume Fribourg, Jean-Jacques Blandin, Pierre Lhuissier, Rémy Dendievel, Guilhem Martin

► **To cite this version:**

Alizée Thomas, Guillaume Fribourg, Jean-Jacques Blandin, Pierre Lhuissier, Rémy Dendievel, et al.. Tailoring the crystallographic texture of pure copper through control of the scanning strategy in Electron Powder Bed Fusion. *Materialia*, 2022, 24, pp.101495. 10.1016/j.mtla.2022.101495. hal-03760679

HAL Id: hal-03760679

<https://hal.science/hal-03760679>

Submitted on 22 Nov 2023

HAL is a multi-disciplinary open access archive for the deposit and dissemination of scientific research documents, whether they are published or not. The documents may come from teaching and research institutions in France or abroad, or from public or private research centers.

L'archive ouverte pluridisciplinaire **HAL**, est destinée au dépôt et à la diffusion de documents scientifiques de niveau recherche, publiés ou non, émanant des établissements d'enseignement et de recherche français ou étrangers, des laboratoires publics ou privés.

Tailoring the crystallographic texture of pure copper through control of the scanning strategy in Electron Powder Bed Fusion

Alizée THOMAS^{1,2}, Guillaume FRIBOURG², Jean-Jacques BLANDIN¹, Pierre LHUISSIER¹,
Rémy DENDIEVEL¹, Guilhem MARTIN^{1,#}

1. Univ. Grenoble Alpes, CNRS, Grenoble INP, SIMAP, F-38000 Grenoble

2. Schneider Electric, Technopole, 28 rue Henri Tarze, Grenoble, France

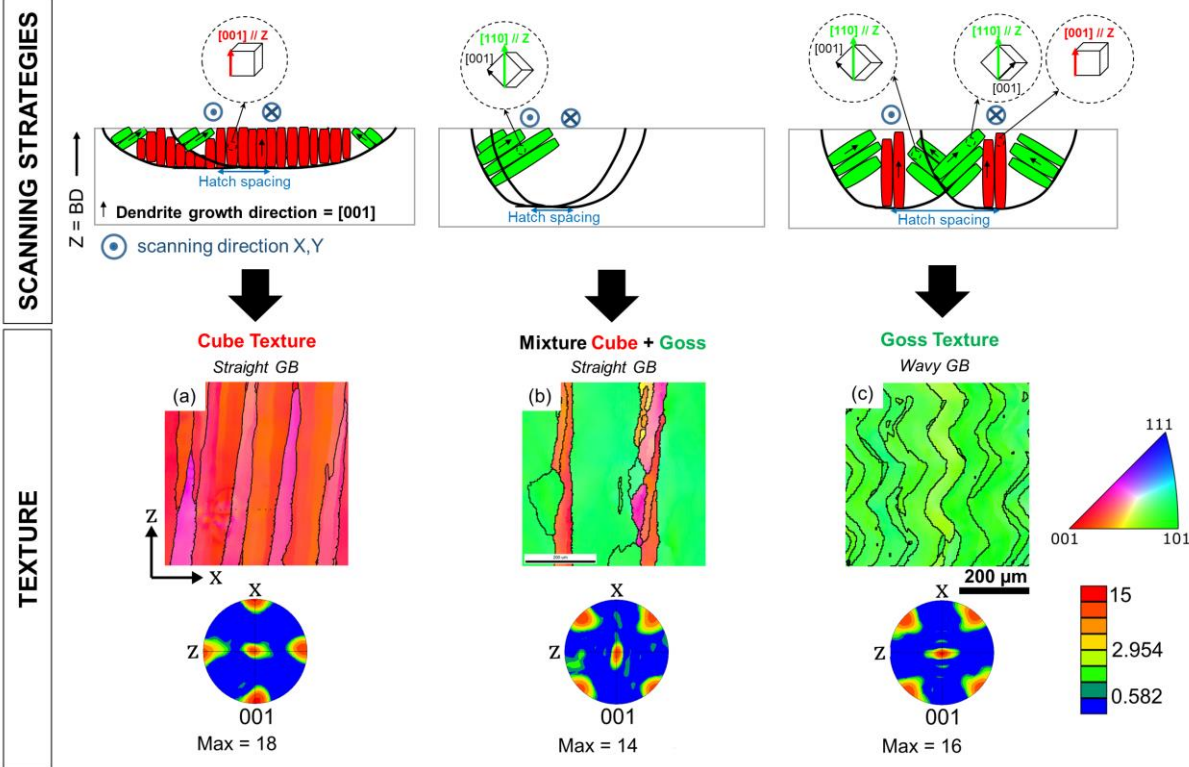
#corresponding author: guilhem.martin@simap.grenoble-inp.fr

Abstract

There has been increasing interest over the past few years to evaluate how additive manufacturing can be used to tailor the microstructure of metallic materials. The objective of this work is to demonstrate through a few illustrative examples the possibility to tailor the crystallographic texture of pure copper processed by Electron Powder Bed Fusion (PBF-EB) by manipulating the molten pool morphology via the scanning strategy. We illustrate schematically how changes in molten pool geometry via modifications of the scanning strategies can affect texture development. Different processing conditions are selected to produce dense samples by PBF-EB while altering the crystallographic texture. The samples produced are examined by optical microscopy and Electron Back-Scattered Diffraction (EBSD) to characterize the molten pool geometry and the inherited microstructure to experimentally validate the pragmatic approach suggested in this work. Manipulations of the scanning strategies are shown to be efficient to produce a strong Cube texture or Goss texture or alternatively, a mixture between the two. A Cube texture is generated by promoting the formation of a melt pool with a flat geometry (its width being much larger than its depth). A Goss texture results from melt pools having a more hemispherical geometry with a large overlap between adjacent tracks. Adjusting the hatch spacing is a good way to achieve a mixture between columnar grains having a Cube texture and others exhibiting a Goss one. The results of this work could be considered as a guideline to tailor the microstructure of other cubic materials processed by PBF-EB.

Keywords: Additive manufacturing; melting strategy; copper; microstructure; EBSD; texture

Graphical Abstract



1. Introduction

Additive manufacturing (AM) first represented a revolution in the world of manufacturing and design by offering new possibilities in terms of part design geometry, see e.g. [1,2]. These new manufacturing techniques have made it possible to produce parts resulting from topological optimization as typically done in [1], often carried out intending to reduce weight. A significant amount of work has been carried out or is still being carried out to improve material quality (internal or surface defects) [3–8], either by optimizing processing conditions [6] or by applying post-treatments, see e.g. [9–14]. Metallurgy has been essentially passively experienced for the time being. The control of microstructures by fully exploiting the processing conditions specific to additive manufacturing is not yet systematically considered but becomes an area of intensive research, see e.g. [15,16]. Modifications of the grain structure: size, morphology, and texture by adjusting the scanning strategies is an interesting pathway to take full advantage of AM-processes because such features can be used to alter the mechanical properties of polycrystalline alloys.

Body-Centered Cubic (BCC) or Face Centered Cubic (FCC) materials processed by Electron Beam Powder bed Fusion (PBF-EB [17]) or Laser Powder Bed Fusion (PBF-LB [17]) tend to often develop a microstructure consisting of relatively coarse columnar grains with their $\langle 001 \rangle$ -direction parallel to the build direction. Strongly textured microstructures have been reported for different alloy families: Ni-based superalloys [18–20], Ti-alloys (based on the reconstruction of the parents β -grains [21–23], Co-Cr alloys [24,25], high entropy alloys [26], austenitic steels [14,27–29]. More recently similar observations were made for pure copper [30].

Over the past few years, there have been intensive research efforts devoted to showing that the strong morphological and crystallographic textures of the grains in parts fabricated by PBF-EB can be altered or modified. This has recently been identified as an area that will require more intensive researches in a recent viewpoint paper, see [31]. The first demonstration of the ability of PBF-EB to produce site-specific controlled microstructures was given in the pioneering work of Dehoff *et al.* [20,32] in a Ni-based superalloy. This was further investigated by different studies, see e.g. [33–36] reporting scanning strategies to produce equiaxed grains with a much weaker morphological and crystallographic texture. Similarly, several research groups reported the possibility to grow single crystals of Ni-based superalloys by selecting appropriate scanning strategies [36–38]. Ramsperger *et al.* went a step further by investigating the creep properties of single crystals grown using PBF-EB [37]. However, investigating ways to tailor the crystallographic texture of pure metals did not receive as much attention although being interesting from a fundamental point of view since the nucleation of grains is significantly reduced in pure metals due to the absence, or a very limited constitutional undercooling.

Pure copper is an interesting material for components such as heat exchangers or electrical conductors. However, pure copper turns out to be difficult to process by PBF-LB using IR-lasers because a large part of the energy input is reflected leading to lack-of-fusion defect (density $<98\%$) and instabilities of the molten pool, see e.g. [39–42]. Less than 5% of the laser beam energy is absorbed by the material when using IR wavelengths [43]. Unlike PBF-LB, PBF-EB was proven to be efficient to build dense parts with relative densities higher than 99.8% [44–47]. The good processability of pure copper using PBF-EB can be accounted for by the good absorptivity of the electron beam energy. The PBF-EB build chamber is under vacuum, and thus can be seen as an additional advantage because parts contamination can lead to a decrease in the electrical conductivity. The possibility to produce dense samples made of pure copper using PBF-EB was reported by several research groups [30,44,46–48]. However, to our knowledge, the effect of the scanning strategy on the microstructure of pure copper fabricated by PBF-EB has not been investigated yet and the possibility to tailor the grain structure is yet to be demonstrated.

In a previous study, we showed that the yield strength and electrical performances of pure copper were not significantly affected by the strong crystallographic and morphological texture inherited from PBF-EB, we only noticed an effect of this strong texture on the work-hardening rate, see [48]. Thus the motivation of this work is not driven by an optimization of the mechanical and/or electrical properties but rather by a need to evaluate how the crystallographic texture of a model FCC-material (pure copper) for which constitutional undercooling is negligible can be modified through changes of the scanning

strategy. As a result, the conclusions drawn in this work could be used to suggest guidelines to tailor the grain structure of other FCC-metals when epitaxial growth is promoted and the nucleation of grains is very limited.

In the present work, we aim at exploiting the processing conditions of Electron Powder Bed Fusion (PBF-EB) to control the melt pool geometry in order to tailor the crystallographic texture of pure copper. We first qualitatively illustrate how changes in molten pool geometry via modifications of the scanning strategy could be employed to alter the crystallographic texture. Different processing conditions are finally retained to produce dense samples by PBF-EB (relative density > 99.9%) while altering the crystallographic texture. The samples produced using the selected processing conditions are examined by optical microscopy and Electron Back-Scattered Diffraction (EBSD) to characterize the molten pool geometry and the inherited microstructure in order to experimentally validate the approach suggested in this work.

2. Conceptual view of the links between molten pool geometry, texture, and scanning strategy

2.1. Role of melt pool geometry on texture development

The objective of this section is to qualitatively illustrate how the molten pool geometry can affect texture development in a pure FCC-metal where dendrites are known to grow preferentially along with one of their $\langle 001 \rangle$ -directions. The molten pool geometry as observed in a transversal cross-section can be described using its aspect ratio (AR) defined as the ratio between the melt pool depth and its width: $AR = d/w$, see **Figure 1a**.

Let us now consider two contrasted situations illustrated with schematics of the transversal cross-sections: on the one hand a “flat” molten pool with a small aspect ratio ($AR \ll 0.3$), see **Figure 1a**; and on the other hand a hemispherical molten pool with a larger aspect ratio ($AR > 0.3$), see **Figure 1b**. The thermal gradient being perpendicular to the solid/liquid interface, one could expect substantial differences in texture development. A molten pool with a small aspect ratio promotes the growth of columnar grains with a $\langle 001 \rangle$ -direction parallel to the build direction (red grains) while a hemispherical molten pool will have a significant portion of columnar grains having a $\langle 110 \rangle$ -direction parallel to the build direction (green grains) because of the grain orientation angle (45° for the $\langle 110 \rangle$ -direction), the latter being defined as the angle between the building direction (BD) and the grain growth direction. We are aware that such schematics are a simplified view of texture development along the molten pool boundary because grain orientation angles between 0 and 90° are theoretically possible but we decided to keep only two grain orientations in for the sake of pedagogy. One should also keep in mind that epitaxial growth from the underlying layers plays a key role in texture development in AM parts, especially for a pure metal for which nucleation of grains is made very difficult due to the absence of constitutional undercooling.

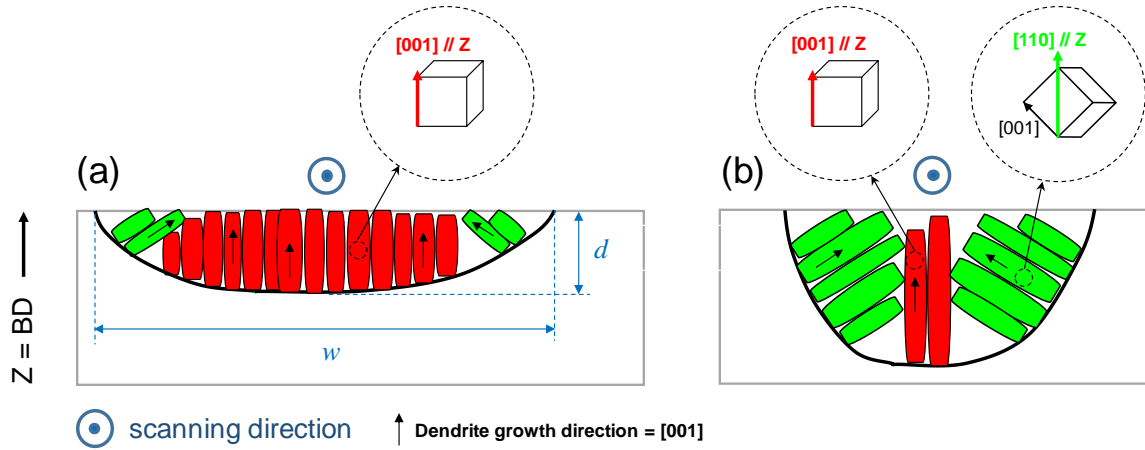


Figure 1. Schematic illustration of the effect of molten pool geometry on texture development (transversal cross-section views). (a) Molten pool with a flat geometry: width much larger than its depth. (b) Molten pool exhibiting a hemispherical morphology.

2.2. Role of hatch spacing on texture development

After having schematically illustrated the role of the molten pool geometry on texture development, we suggest now examining how the hatch spacing, i.e. the distance between adjacent molten tracks can be used to control the texture in parts processed by PBF-EB. Two cases will be considered, once again illustrated with schematics of the transversal cross-section view of the molten pool: a small hatch spacing and a large hatch spacing for respectively a flat molten pool (**Figure 2 (a-b)**), and a hemispherical one (**Figure 2 (c-d)**).

The schematics displayed in **Figure 2 (a-b)** show that in the case where the molten pool is extended in the direction perpendicular to the scanning direction, the hatch spacing has nearly no effect on the resulting texture. Indeed, regardless of the imposed hatch spacing, most of the grains will be oriented such as one of their $\langle 001 \rangle$ -direction is parallel to the build direction. The addition of layers will promote epitaxial growth (promoted in the case of pure Cu because nucleation is very difficult due to the absence of constitutional undercooling) and the few grains with a growth direction tilted with respect to the build in the overlap area between two adjacent tracks (green grains) will disappear for the benefit of red grains, i.e. grains with a $\langle 001 \rangle$ -direction parallel to the build direction.

As illustrated in **Figure 1 (b)**, the formation of a hemispherical molten pool enables to change the texture by promoting the formation of grains with a $\langle 110 \rangle$ -direction parallel to the build direction (green grains) at the expense of the grains with a $\langle 001 \rangle$ -direction parallel to the build direction (red grains). In addition, **Figure 2 (c-d)** shows that when a more hemispherical molten pool geometry is achieved, hatch spacing can be tuned to control the proportion of $\langle 001 \rangle$ -oriented grains. Ultimately, the presence of red grains can even be suppressed when imposing a small enough hatch spacing as shown in **Figure 2 (d)**. In the latter case, the side branching mechanism is exploited in the overlap region between adjacent tracks to preserve the $\langle 110 \rangle$ -oriented grains. Side branching is defined as a mechanism allowing the growth of grains along with orthogonal directions in response to changes in local heat flux, see [49] for more details. The region where side-branching occurs is highlighted by the gray area in **Figure 2 (c)**.

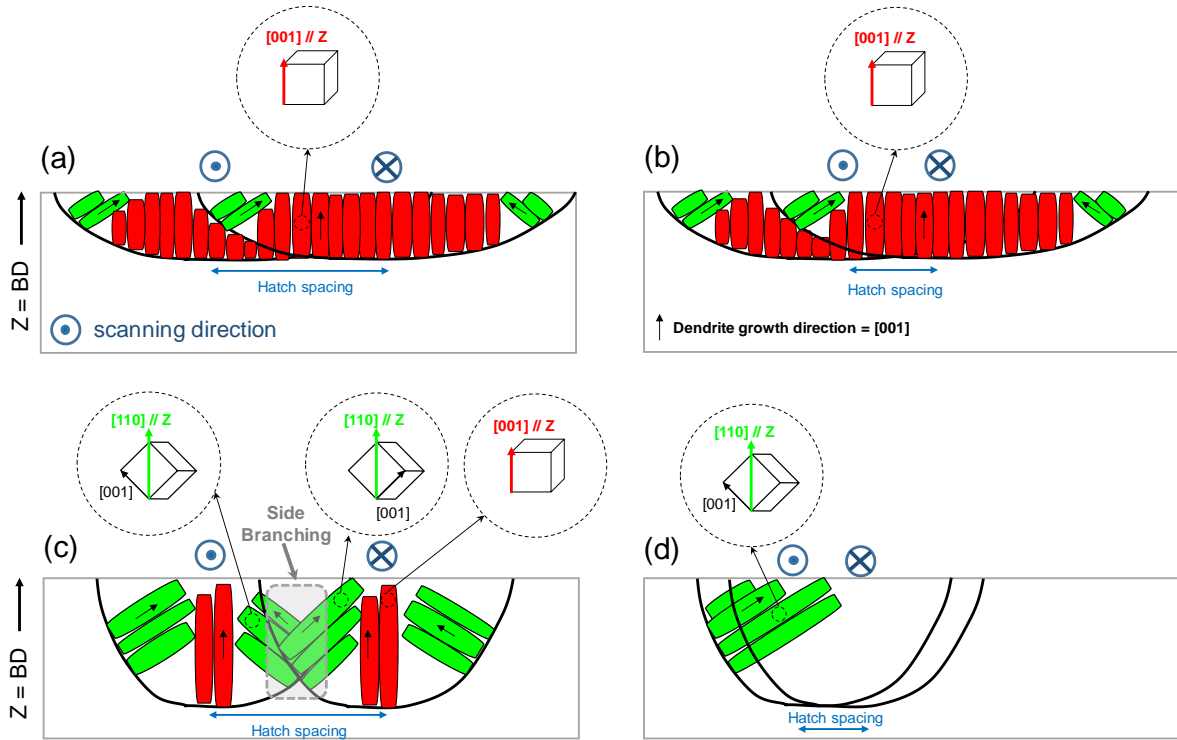


Figure 2. Schematic illustrating the effect of hatch spacing on texture development for (a-b) a molten pool spread in the direction perpendicular to the scanning direction (cross-section views), and (c-d) a molten pool exhibiting a hemispherical morphology (cross-section view). Red grains are grains having a $\langle 001 \rangle$ -direction parallel to the build direction while green grains are tilted with respect to the build direction.

2.3. Role of the scanning strategy on the molten pool geometry

Now that we have qualitatively established the relationships between the melt pool morphology and texture development, one needs to think about the links between the processing conditions including melting parameters and scanning strategy, and the resulting melt pool morphology. Based on simple considerations supported by the published literature [34,50–52] regarding the effect of the processing conditions on the molten pool size and morphology, we illustrate hereafter using schematics how changes in beam power or speed while using a snake-like hatching pattern can affect the melt pool geometry. Similarly, the case of a spiral-like molten pool geometry will be considered. Such simple considerations will be then used to guide the processing conditions that will be retained to produce dense pure copper samples with specific crystallographic textures.

2.3.1. Snake-like scanning strategy: effect of beam power and speed

We illustrate with the help of simple schematics how changes in first-order melting parameters, namely power and scan speed, can result in drastically different molten pool morphologies. This is important because we conceptually showed in sections 2.1 and 2.2. how the molten pool morphology and hatch spacing can be tuned to alter the crystallographic texture.

A schematic illustrative example of the effect of the first order melting parameters while using a snake-like scanning strategy is given in **Figure 3** where top views (building direction pointing to the reader) are shown to appreciate differences in molten pool geometry induced by an increase of beam power or beam speed. The scanning strategy chosen here is the most widely employed scanning pattern in PBF-EB, i.e. a snake-like hatching strategy. For a given power, one needs to select a not too high scan speed to extend the melt pool perpendicularly to the scanning direction. Similarly, for a given scan speed, an increase of power is desired to promote the spread of the melt pool perpendicularly to the scanning direction. From **Figure 3**, it is rather clear that the melt pool shape varies greatly depending

on the processing parameters applied, ranging from a point source, typically the cases illustrated in **Figure 3 (a, d, g)** to very large and stretched shapes as exemplified in **Figure 3 (b, c)** and **(f, i)**. This situation is sometimes described in the literature as the difference between a point heat source that leads to the formation of a tear-drop shape molten pool and a line heat source that gives much larger molten pools, see e.g. [53][50]. In PBF-EB, the molten pool geometry (i.e. the aspect ratio) can be more easily changed in comparison with PBF-LB. Indeed, the combination of both preheating and relatively high scanning speeds lead to the formation of large molten pools elongated in the direction perpendicular to the scanning tracks because the heat generated while melting a given track does not have enough time to be fully released when the electron beam melts adjacent lines, see e.g. [50,53,54][51]. In other words, this means that the molten pool geometry depends on the time required to release the heat generated by the preceding track. In the time required for scanning, the heat-induced by the preceding track diffuses into the substrate by heat conduction, if the time between two adjacent tracks is not long enough, it will promote the formation of large molten pools stretched in the direction perpendicular to the scanning direction [51,52,54] (**Figure 3 (b, c)** and **(f, i)**). On the opposite, if the time is long enough then hemispherical molten pools (as observed in transversal cross-sections) will be promoted (**Figure 3 (a, d, g, h)**). Note that depending on the physical properties of the material fabricated the molten pool can be even more elongated in the direction perpendicular to the scanning tracks. Here, pure copper has a very high thermal conductivity but with the processing parameters and a snake-like scanning strategy, it is still possible to achieve a melt pool propagating through several adjacent lines. Metals and alloys having thermal conductivities lower than pure copper such as superalloys, and to a larger extent, Ti-alloys are known to develop even larger molten pools, see e.g. [50,53,54].

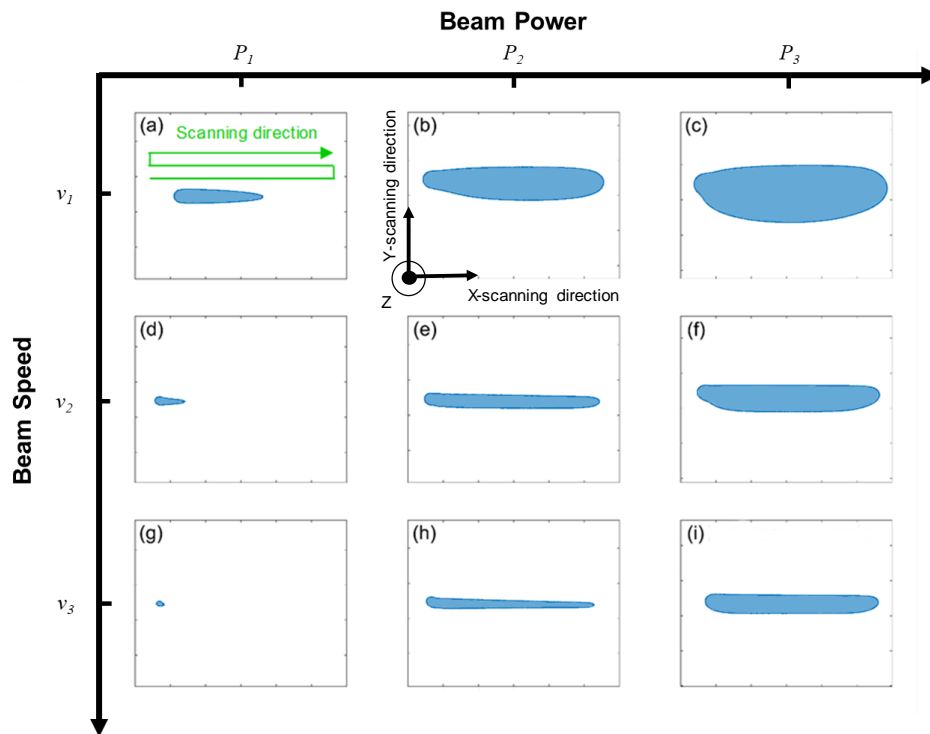


Figure 3. Schematic top views (building direction perpendicular to the plane of observation) illustrating the influence of beam power and scan speed on the molten pool morphology in the stationary regime. Here $P_1 > P_2 > P_3$ and $v_1 > v_2 > v_3$.

2.3.2. Spiral-like strategy

We have also considered the peculiar case of a spiral scanning strategy because the time between two adjacent tracks will continuously increase as the beam gets further from the center. The situation shown in **Figure 4** allows the change of molten pool geometry to be schematically and qualitatively appreciated in the case of a spiral-like scanning strategy. When melting the first few spiral patterns at the center, the time to completely release the residual heat of the previous pattern is expected to be not

long enough resulting in a large square-shape molten pool as illustrated in **Figure 4a**. While getting further from the center, the time required to release the heat-induced by a given track when melting the adjacent line becomes long enough so that a hemispherical molten pool is promoted, see **Figure 4b**. Thus, we can take advantage of a spiral scanning strategy to evaluate with a single sample the effect of this critical time on the molten pool morphology. Indeed, evaluating the effect of this critical time using a snake-like scanning pattern will require producing cubes with different sets of melting parameters (power and scan speed) as shown in **Figure 3**.

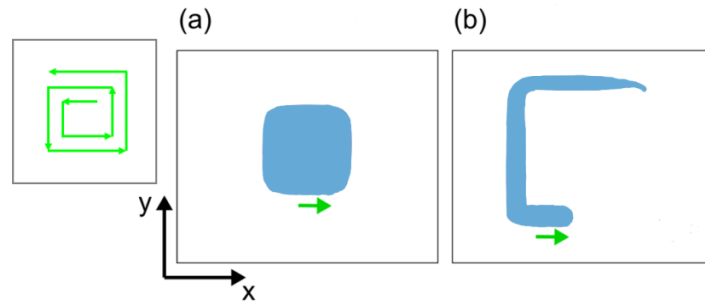


Figure 4. Schematic top views illustrating the morphology of the melt pool when using a spiral-like scanning strategy. (a) Molten pool morphology after scanning the first few spiral patterns at the center. (b) Molten pool morphology when scanning spiral patterns further away from the center.

We will now rely on our conceptual views of the relationships between the molten pool morphology and texture development (**Figure 1** and **Figure 2**) and between the melting parameters or scanning strategy and the molten pool morphology (**Figure 3** and **Figure 4**) to guide the selection of processing conditions that lead to drastically different textures. However, such guidelines remain qualitative and therefore still require experimental validations to ensure the fabrication of dense samples to avoid porous samples or on the contrary overmelted samples. Numerical approaches could be further employed in the future to strengthen the pragmatic approach suggested in this work as it would possibly offer the opportunity to quantitatively guide the selection of some processing conditions, thus speeding up the subsequent experimental optimization of the processing conditions. The processing conditions that were finally employed to experimentally validate our approach to tailor the microstructure of pure copper fabricated by PBF-EB will be detailed in section 3.2.

3. Experimental procedures

3.1. Materials and PBF-EB fabrication

The copper powder was produced by gas atomization (argon) from Oxygen-free copper (Cu-OF) rods with 25 ppm of oxygen. The composition of the copper powder meets the requirement for Cu-ETP grade (99.93 %wt in Cu), with 0.011 %wt O, 0.005 %wt Ti, %wt of P < 0.005, and 1 ppm of H. A more detailed analysis of the chemical composition of the powder batch is given in [48]. The powder was loaded into a PBF-EB machine from ARCAM (A1 machine controlled by the software EBM Control 3.2 operating under vacuum ($2 \cdot 10^{-3}$ mbar) and at an accelerating voltage of 60 kV. The automatic mode of the software EBM Control 3.2 that controls the beam parameters was disabled. This is important because when the automatic mode is turned on, different functions are activated to control the electron beam to improve the build quality for sophisticated geometries by adjusting the beam parameters (power, scan speed) to locally vary melting conditions as a function of the scan lengths or the presence of negative surfaces.

A homemade miniaturized building chamber that fits into the ARCAM-A1 standard building chamber was used in this study. $70 \times 70 \times 10$ mm³ start plates made of Cu-ETP were used. The preheating area was kept constant for all experiments: 60×60 mm² and was performed using a defocused beam (focus offset set to 100 mA). On the contrary, a focused beam was used to melt the powder bed. Parallelepipedic samples were built with an edge length of 10 mm and a height of 15 mm using the different scanning strategies that will be detailed in the next section entitled “Selected scanning strategies”. Throughout the manuscript, (x,y,z) refer to the coordinate system of the building substrate: x and y being the scanning directions, and z the building direction (BD).

3.2. Selected scanning strategies

Based on the schematics shown in **Figure 1** and **Figure 2**, we selected different processing conditions that ensured the fabrication of dense samples (relative density > 99.9%) while allowing the crystallographic texture to be modified. Simple thermal calculations using analytical solutions such as the Rosenthal model, see e.g. [49,52,55] could have been used to guide the selection of the processing parameters but this is not what has been done in this work. Here, the selection of the processing parameters finally retained were empirically determined by conducting design of experiments for the various scanning strategies investigated but with variations of the beam power and speed. The relative density and melt pool geometry were systematically examined to guide our final selection. The detailed processing conditions used to produce the different samples selected for further analyses are given in **Table 1**. Those samples are used to provide several experimental validations of the simple approach suggested in this work in section 2. It is important to emphasize that the different samples selected were not necessarily produced in the same build. Thus, the preheating temperature applied to produce the samples retained in this work is not necessarily the same. As a general rule of thumb, increasing the preheating temperature with a given scanning strategy promotes the formation of large molten pools that get extended perpendicularly to the scanning direction (i.e. $AR < 0.3$). Copper, also known to be a non-smoke sensitive material due to a combination of high density and high electrical conductivity, can be processed using significant variations of the preheating temperatures from 380°C to 600°C [47,56]. On the opposite, the range of preheating temperatures required to produce samples made of Ti-alloys is not as wide.

Scanning strategy (1) was chosen to achieve a strong Cube texture. A Cube texture corresponds to the case where grains are oriented such as they have a <001>-direction parallel to the building direction and the two others <001>-directions aligned with the scanning directions x and y. Scanning strategy (2) allows the development of a mixture between grains with a Cube texture and grains exhibiting a Goss texture while scanning strategy (3) was retained to promote the formation of a strong Goss texture. A Goss texture corresponds to the case where grains are oriented such as they have a <110>-direction parallel to the building direction while one of the <001>-direction remains parallel to one of the scanning

directions x or y. This terminology to qualify a texture: Cube or Goss was adapted from the literature regarding texture development in processing routes involving plastic deformation, see e.g. [57].

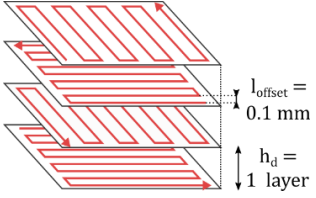
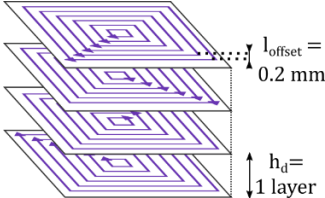
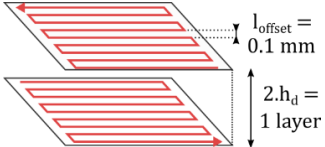
# Scanning strategy	T_{preheat} (°C)	Scanning speed (mm/s)	Beam Power (W)	Line offset (mm)	Hatch depth (μm)	Layer thickness (μm)
(1) Cube Texture 	550	3000	1200	0.1	50	50
(2) Goss Texture 	410	1300	1200	0.25	NA	50
(3) Goss texture and grain boundary morphology 	460	350	600	0.1	50	100

Table 1 : Overview of the various scanning strategies along with the associated processing parameters employed to tailor the microstructure and microtexture. Scanning strategy (2) consists in using the contour strategy available in EBM Control 3.2. with the multisport option disabled. Line offset corresponds to the so called hatch spacing, i.e. to the distance between two adjacent tracks. Hatch depth indicates the frequency of the rotation of the scanning direction. For example, a hatch depth of 50 μm means that the scanning pattern is rotated at each layer for a layer thickness of 50 μm . A hatch depth of 50 μm when the layer thickness is taken equal to 100 μm means a rotation of the scanning pattern by 180° at each layer.

3.3. Microstructural characterization

Samples for metallography were subjected to the following preparation stages starting with grinding from 800 down to 2400 using SiC abrasive papers and polishing with 3 and 1 μm diamond suspensions. Due to the high ductility of copper, porosity in the sample can be filled in during grinding and polishing. Thus, an additional chemical polishing step was carried out using a solution consisting of 100 mL H_2O , 100 ml ethanol, and 19 g of iron (III) nitride as a lubricant. This chemical treatment helps to clear out the pores as well as reveal the grain boundaries. However, as such a chemical polishing also reveals the grain boundaries, estimating the porosity required a final gentle polishing using the 1 μm diamond suspension. The latter operation allowed the etching effects to be removed without filling the pores. Optical micrographs were then taken with an Olympus DSX 510 opto-numerical microscope. Note that revealing the melt pool boundaries is not always straightforward in materials processed by PBF-EB, most likely because the material undergoes an in-situ heat treatment during the process due to the preheating stage. This in situ heat treatment is thought to homogenize the microstructure making challenging the detection of the melt pool boundaries. Here, as we are working with a metal exhibiting a relatively high purity, this can make the identification of the melt pool boundaries even more difficult. For a sake of clarity, we intentionally have highlighted at least some melt pool boundaries in the etched micrographs shown in the subsequent sections.

The melt pool geometry, namely its aspect ratio (AR), was characterized by measuring its depth, d , and half-width, w ($AR = d/(2 \times w)$) in optical micrographs taken perpendicularly to the scanning direction, see example in **Figure 5**. At least ten measurements for the depth and half-width were made and the average value was retained, the error is estimated by computing the standard deviation.

For Scanning Electron Microscopy (SEM) observations, samples were mechanically polished down to 1 μm with a diamond suspension and then electropolished in a 65% aqueous phosphoric acid solution. The electropolishing conditions were set at 5 V and 2 mA for 120 seconds with a stainless-steel cathode. SEM images were acquired with a ZEISS GEMINI SEM500 with an operating voltage of 15 kV. For EBSD analysis, a step size varying from 2 to 5 μm was employed. Electron Backscatter Diffraction (EBSD) maps were post-treated using the OIM Analysis software. The grain widths were measured using the intercept method with lines drawn perpendicularly to the build direction (BD).

4. Results and discussion

4.1. Promoting a strong Cube texture

We recall here that a Cube texture is achieved when the grains show one of their $\langle 001 \rangle$ -directions parallel to the build direction while two others $\langle 001 \rangle$ -directions are aligned with the scanning directions x and y . To achieve a microstructure consisting of columnar grains exhibiting a strong Cube texture, we need to promote a line heat source that leads to the formation of a large molten pool that spreads along the direction perpendicular to the scanning direction.

We decided to produce a sample using a relatively high power (P set to 1200 W) and a not too high scan speed (v fixed at 3000 mm/s) to promote the formation of a large molten pool extending in the direction perpendicular to the scanning direction mimicking a situation close to the one shown schematically in **Figure 3 (f, i)**. The scanning strategy employed here is the most widely employed scanning pattern in PBF-EB: a snake-like strategy with a 90° rotation of the scanning pattern at each layer. The hatch spacing was set to 0.1 mm (Line offset) and the layer thickness was constant throughout the build and set to 50 μm . Based on previous work, we knew that such processing conditions allow dense samples to be produced consistently since the relative density of such samples was measured to be higher than 99.95% by both X-ray computed tomography and image analysis, see [48]. Those melting conditions are summarized in **Table 1**. This optimized set of parameters is also consistent with the processing window identified in another recent publication, see [19].

An overview of the microstructure inherited from scanning strategy (1) is given in **Figure 5**. A homogeneous microstructure was found from the bottom to the top of the 15 mm-height samples. The EBSD-IPF map normal to the build direction (BD) and the associated pole figures are shown respectively in **Figures 5 (a)** and **(b)**. This microstructure consists of columnar grains elongated along the build direction with an average width measured with the intercept method of nearly 50 μm . As targeted, a strong Cube texture is evidenced by the pole figures shown in **Figure 5 (b)**, the $\langle 001 \rangle$ -directions being aligned along the build direction ($\text{BD} = z$) as well as along both scanning directions (x and y) with a maximum intensity close to 15.

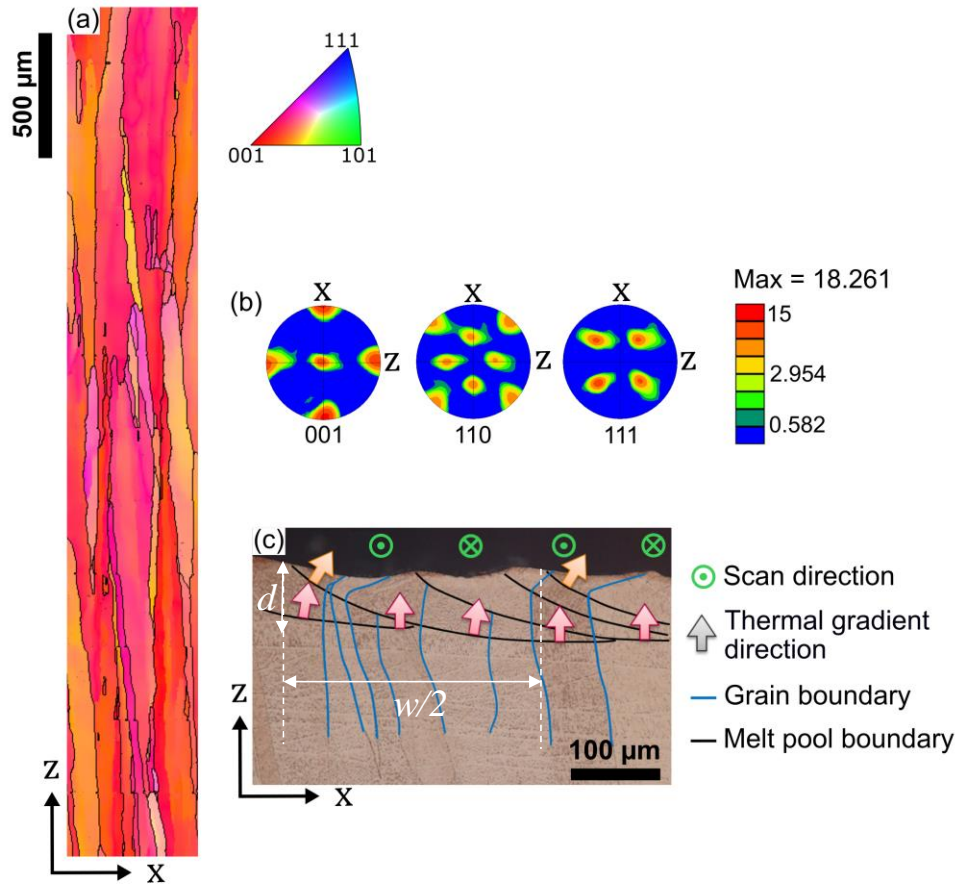


Figure 5 : (a) EBSD IPF-Z map acquired in the xz -plane of a sample produced using the standard snake-like scanning strategy (processing parameters given in **Table 1**) where grain boundaries are displayed in black and are associated with interfaces having a misorientation angle $> 15^\circ$. (b) (001), (110) and (111) Pole figures, (c) Optical micrograph of the topmost layer, grain boundaries are highlighted in blue while melt pool boundaries appear in black (x,y,z) is the coordinate system with x and y being the scanning directions, and z the build direction (BD).

Observations of the topmost layer of a part fabricated using the standard snake-like scanning strategy (details of the processing conditions provided in **Table 1**) have been carried out to assess that the molten pool geometry was indeed stretched in the direction perpendicular to the scanning direction. Grain and melt pool boundaries were revealed by chemical etching and are respectively highlighted using black and blue lines in **Figure 5 (c)**. The molten pool aspect ratio (AR) was roughly estimated by measuring its depth, d , and half-width, w ($AR = d/(2 \times w)$) as indicated in **Figure 5 (c)**. The melt pool depth was measured to be about $d = 70 \pm 8 \mu\text{m}$ and the width $w = 2 \times 250 = 500 \pm 10 \mu\text{m}$. For the selected processing parameters, the melt pool exhibits a relatively flat morphology ($AR = 0.15$) as shown in **Figure 5 (c)** suggesting that it is indeed elongated in the direction perpendicular to the scanning direction, see **Figure 2 (a-b)**. The molten pool depth being 1.5 times larger than the layer thickness, promotes the epitaxial crystal growth leading to columnar grains propagating through several layers and elongating over several hundreds of microns. This first illustrative example can be considered as the first experimental validation of the simple approach proposed in this work.

Scanning strategy (1) leads to a strong Cube texture, see **Figure 5 (a)**. Similar strong Cube textures have been produced in different cubic materials processed by PBF-EB, see e.g. examples in Ni-based superalloys [18,34,35,38], Co-Cr-Mo alloys [25], and CrMnNi steel [27]. Interestingly, in microstructures inherited from PBF-LB, it turns out to be more difficult to produce such strong Cube textures because large melt pools stretched in the direction perpendicular to the scanning strategy as schematically illustrated in **Figure 1 (a)** and in **Figure 3 (b)** (for a cross-section view and a top view, respectively) are very difficult to achieve in PBF-LB. This has to do with the absence of preheating and slower scanning speeds in PBF-LB in comparison with PBF-EB. The formation of such large melt pools

in PBF-EB partly explain why different groups have successfully grown single crystals by PBF-EB [38,58,59]. It is also interesting to highlight that in PBF-LB, the melt pool morphology often shows a hemispherical morphology but can relatively easily be modified by substantially increasing the energy input to be in a keyhole regime where the melt pool depth becomes much larger than its width (exactly the opposite situation as the one selected here to produce a Cube texture). Achieving a keyhole regime with the PBF-EB machines currently available is relatively difficult (accelerating voltage of 60 kV). In summary, one could say that PBF-EB enables to achieve flat melt pools with small AR (< 0.3), this cannot be easily done in PBF-LB. On the opposite, large AR (> 1) can be easily achieved in PBF-LB but this is very challenging to do in PBF-EB, at least with the current generation of machines.

The objective was then to apply scanning strategies allowing to alter this Cube texture and ultimately to produce a Goss texture, i.e. grains having one of their $\langle 110 \rangle$ -directions parallel to the build direction (green grains in the schematics shown in **Figure 2 (c)**). To do so, we need (i) to select conditions that lead to a hemispherical molten pool geometry, and (ii) to adjust the hatch spacing to control the proportion of green grains and red grains as shown in **Figure 2 (c-d)**.

4.2. Producing a mixture of Cube and Goss texture

To reproduce the situation represented in **Figure 2 (c)**, we employed a spiral scanning pattern consisting of scanning the surface concentrically from the center towards the edges (inner to outer beam trajectory) as typically shown in **Table 1** – strategy (2). A relatively large line offset, set to 0.25 mm (more than twice the one used for the sample produced using a standard snake-like strategy) was employed. Power and scan speed were adjusted to achieve a relative density above 99.5%. When using a constant scan speed when applying such a strategy, a change in molten pool geometry is expected because the time between adjacent tracks will continuously increase when getting closer to the edges, see the schematic of the top view of the melt pool in **Figure 4**.

The EBSD-IPF map acquired over the whole width (**Figure 6**) of the sample reveals the presence of two different microstructures depending on the location: a first microstructure consisting of two very large grains at the center of the sample, and a periodic arrangement consisting of wide columnar grains with the $\langle 110 \rangle$ -direction parallel to the build direction and thinner columnar grains with their $\langle 100 \rangle$ -direction parallel to the build direction near the edges. The microstructure observed near the edges is very similar to the situation schematically represented in **Figure 2(c)**. As a result, we suggest first focusing on the microstructure observed near the edges as it corresponds to the one desired. The difference between the center and the edges will be discussed later.

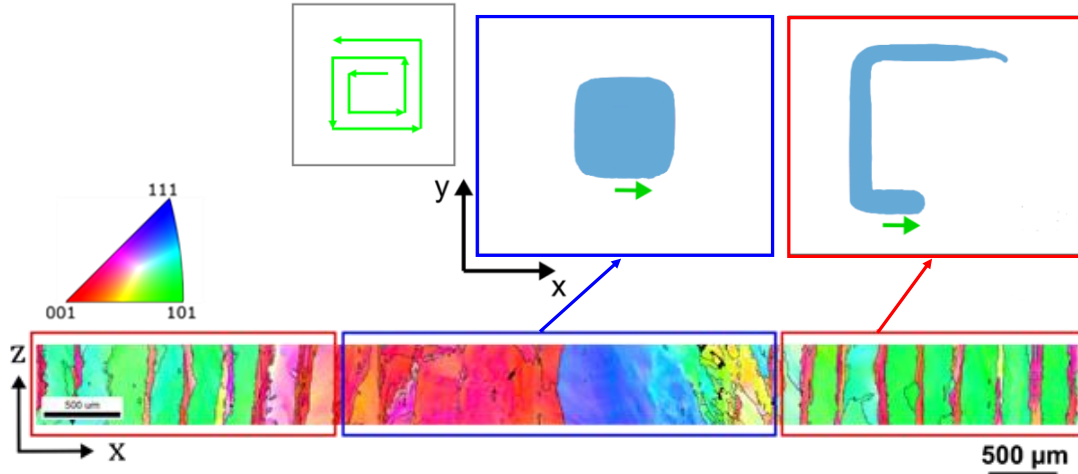


Figure 6: Grain structure inherited from a spiral-like scanning strategy and characterized by EBSD in the XZ-plane, Z being parallel to the build direction. Schematic top views of the molten pool morphology associated to different region of interest along the width of the sample fabricated using a spiral-like strategy.

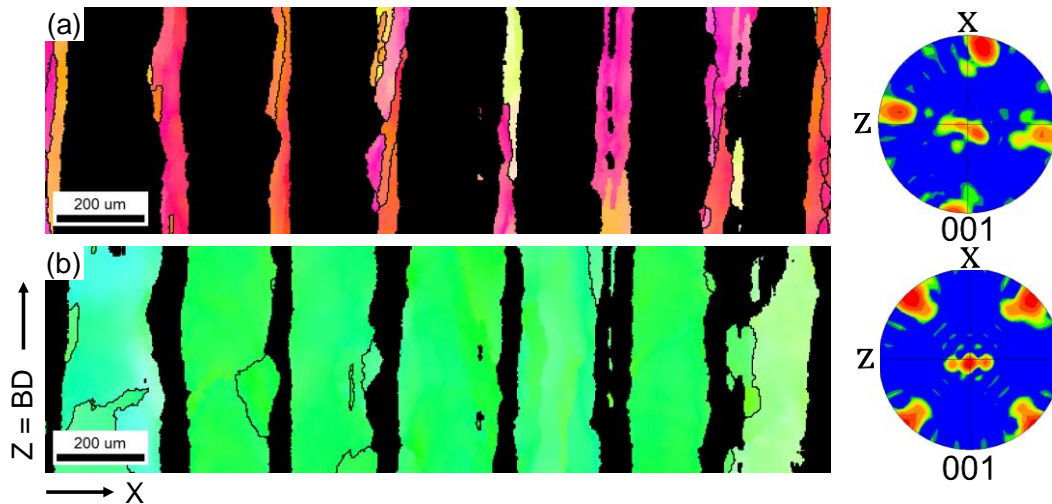


Figure 7. (a) EBSD-IPF map highlighting grains with a misorientation angle $< 15^\circ$ with respect to the $\langle 001 \rangle$ -direction and corresponding (001) pole Figure. (b) EBSD-IPF map highlighting grains with a misorientation angle $< 15^\circ$ with respect to the $\langle 110 \rangle$ -direction and corresponding (001) pole Figure.

The microstructure of the sample built with scanning strategy (2) is a mixture of grains with a Cube texture (**Figure 7a**) and grains showing a Goss texture (**Figure 7b**). The formation of the alternating Goss-Cube textured columnar grains can be accounted for based on the examination of the melt pool shape revealed by optical microscopy. In **Figure 8**, the melt pool shape obtained with scanning strategy (2) is compared with the one resulting from the snake-like scanning strategy (1). Based on the optical micrographs of the topmost layer, see **Figures 8 (a) and (b)**, the melt pool boundaries are observed in the xz-plane. These boundaries are illustrated in **Figures 8 (c) and (d)** along with the thermal gradient directions (see arrows in **Figure 8 (c-d)**). In comparison with the microstructure inherited from the scanning strategy (1), scanning strategy (2) leads to a larger aspect ratio, $AR \sim 0.34$ vs 0.15 for the scanning strategy (1). **Figure 8 (c-d)** shows the influence of the change of the melting strategy on the melt pool morphology and thus the thermal gradient orientation. Indeed, in presence of a more hemispherical molten pool with deeper edges, the thermal gradient direction along the solidification front is significantly modified, from 0° (bottom) to 45° (edge) with respect to the BD.

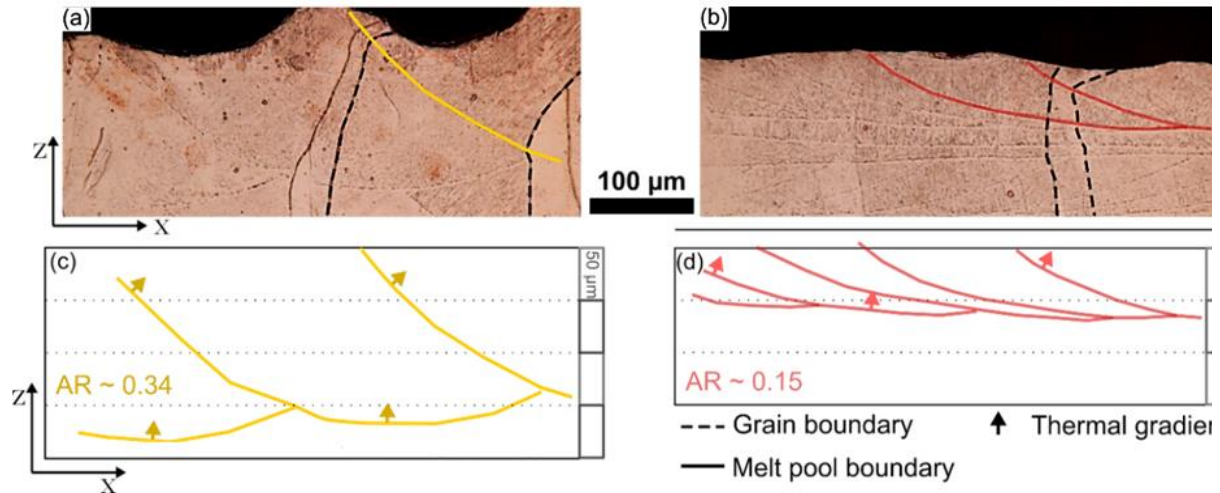


Figure 8 : Optical micrographs of (a) the sample built with the scanning strategy (2) and (b) the sample fabricated using scanning strategy (1) where both the grain and the melt pool boundaries have been revealed by chemical etching. Schematic illustrations of the melt pool shape of (c) the new sample and (d) the sample fabricated using scanning strategy (1). Those illustrations are based on the optical micrographs presented above. The thermal gradient directions, perpendicular to the solid/liquid interface, are indicated with arrows.

To link the melt pool shape with the resulting microstructure, an optical micrograph and an EBSD-IPF map are shown in **Figure 9**. On the optical micrograph shown in **Figure 9 (a)**, six melt pool boundaries are highlighted in black, the thermal gradient orientations are indicated with arrows. The thin red grains ($\langle 001 \rangle$ -direction parallel to the build direction) are located at the center of the melt pools whereas the larger green grains ($\langle 110 \rangle$ -directions parallel to the build direction) are located near the edges. These melt pool boundaries are then superimposed onto the EBSD-IPF map, see **Figure 9 (b)**. At the center of the melt pool, the thermal gradient is mainly parallel to the build direction. Thus, at this location, columnar grains with a Cube texture grow epitaxially along the build direction. This is consistent with the fact that the periodicity of the texture is approximately 0.25 mm, exactly the imposed hatch spacing (line offset). This crystal growth direction is also promoted thanks to a relatively small overlap between adjacent molten tracks. Indeed, the melt pool center is not remelted while melting the adjacent scanning track, but only while processing the next layer with melt pools stacked on each other along the build direction. At the edges of the melt pool, the same mechanism operates, however, in this case, the thermal gradient is oriented at nearly 45° with respect to the build direction according to the steep edges of the melt pool. The grains grow in epitaxy but with the $\langle 110 \rangle$ -direction being aligned with the build direction. Note that the thermal gradient and consequently the preferential crystal growth direction, exhibit the same direction in all layers because the melt pools are stacked on top of each other without changing the scanning pattern orientation. For both columnar grain orientations (red and green grains in **Figure 9 (b)**), the epitaxial growth is promoted because about 2-3 layers are remelted and the thermal gradient direction is preserved between successive layers.

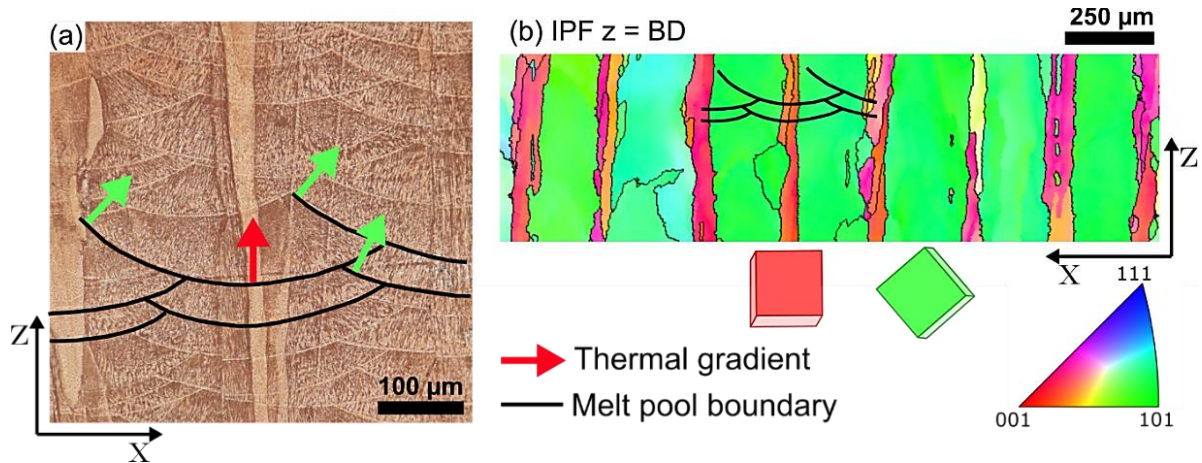


Figure 9 : (a) Optical micrograph of the sample built with scanning strategy (2), where the melt pool and grain boundaries were revealed by chemical etching. 6 melt pool boundaries are highlighted with black lines, and some selected thermal gradient orientations are represented with arrows. (b) EBSD-IPF map representing the grain orientation normal to the build direction. Two populations of grain orientations are observed: the red grains with a texture (Cube texture), and the green grains with a texture (Goss texture). The melt pool boundaries are superimposed from the optical micrograph to the EBSD-map.

The opposite scanning strategy, i.e. melting from the edges to the center of the surface (Outer to Inner scanning strategy), has also been studied. The resulting microstructure is very similar to the sample studied here as shown in **Figures 10 (a)** and **(b)**.

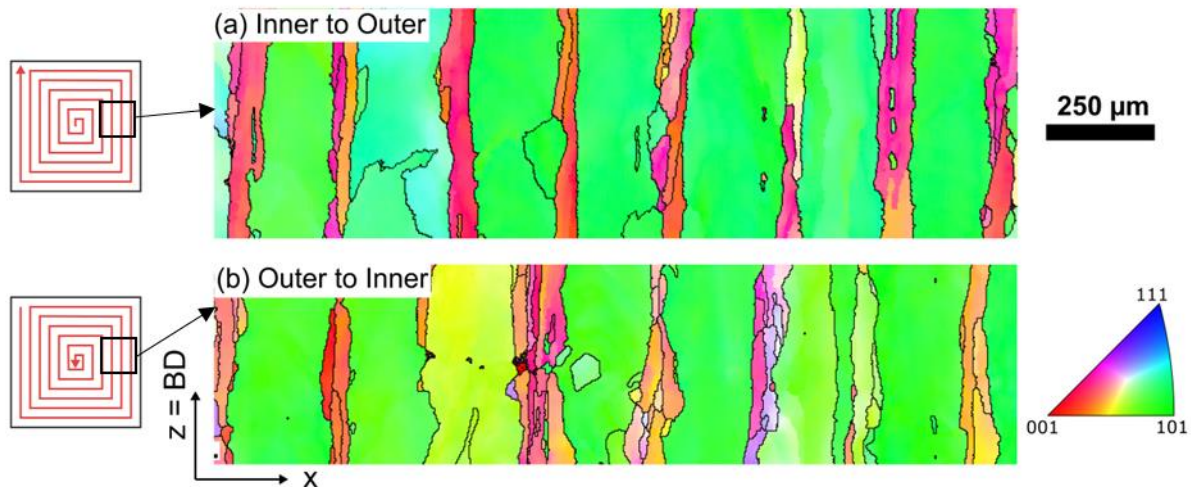


Figure 10. EBSD-IPF maps normal to the build direction acquired near the edges in (a) a sample built with the scanning strategy (2) (Inner to Outer) and (b) a sample produced with the same set of parameters but from Outer to Inner. Grain boundaries are displayed in black and are associated with interfaces having a misorientation angle $> 15^\circ$.

The differences in grain structure between the center and the edges can be rationalized based on the simple thermal considerations shown in **Figure 4**. Two regimes can be distinguished when using the scanning strategy (2). For the first squares (center), the melt pool is stretched over the adjacent lines leading to a large square-shaped molten pool with a very small aspect ratio because there is not enough time to completely release the heat generated by the preceding line (**Figure 4 (a)**). This situation results in the formation of two large grains on either side of the center of the sample. When getting closer to the edges, there is enough time to release the heat generated by the previous tracks leading to the formation of a more hemispherical melt pool along the beam trajectory, see **Figure 4 (b)**.

To summarize, the crystallographic texture has been successfully changed from a strong Cube texture to a microstructure consisting mostly of columnar grains showing a Goss texture and a few other columnar grains with a Cube texture. Interestingly, this microstructure mimics a lot of situations found in the PBF-LB literature dealing with the fabrication of different cubic materials [14,26,28], in particular studies dedicated to austenitic stainless steels, see e.g. [28,29,60]. Note that there would be different ways to produce such a microstructure and that one needs to promote hemispherical melt pools, something that can be easily done in both PBF-EB and PBF-LB. One option would consist in applying the snake-like scanning strategy but by increasing the line offset and suppressing the rotation of the scanning direction at every layer or imposing one of 180° so that the molten tracks stack on top of each other between successive layers as done in the study of Andreau *et al.* using PBF-LB [28].

4.3. Promoting a strong Goss texture

To reproduce the situation shown in **Figure 2 (d)**, we needed to (i) promote the formation of a hemispherical molten pool geometry and (ii) apply a reduced hatch spacing to suppress the formation of grains exhibiting a Cube texture (red grains). This was achieved using the scanning strategy (3). Here the layer thickness was set to $100\ \mu\text{m}$. The hatch depth was set to $50\ \mu\text{m}$ (i.e. 0.5 layers), meaning that the scanning pattern was rotated by 180° at each layer while it was 90° for the scanning strategy (1). The melting parameters (power and scan speed indicated in **Table 1**) were optimized to produce samples with a relative density $> 99.5\%$.

The microstructure resulting from the scanning strategy (3) is shown in **Figure 11**. The EBSD-IPF map shows that the inherited microstructure is strongly textured with the $\langle 110 \rangle$ -direction aligned with the build direction (Goss texture, see **Figure 11 (a-b)**). Note, in contrast with the microstructure shown in **Figure 10 (a-b)**, the absence of columnar grains having their $\langle 001 \rangle$ -direction parallel to the build direction. This has been made possible by drastically reducing the hatch spacing resulting in a large overlap between two adjacent tracks as schematically shown in **Figure 2 (d)**. An additional consequence of the use of the scanning strategy (3) is the waviness character of the grain boundaries (**Figure 11 (a)**) that contrast with the relatively straight boundaries observed in the specimens shown in (**Figure 5 (a)**) or **Figure 10 (a-b)**. This was caused by the 180° rotation of the scanning direction at each layer. The wavelength of this microstructure is about $200\ \mu\text{m}$ which corresponds exactly to twice the layer thickness applied to produce this specimen. The average columnar grain width measured using the intercept method is about $45\ \mu\text{m}$ on average with some grains having a length as long as 3 mm.

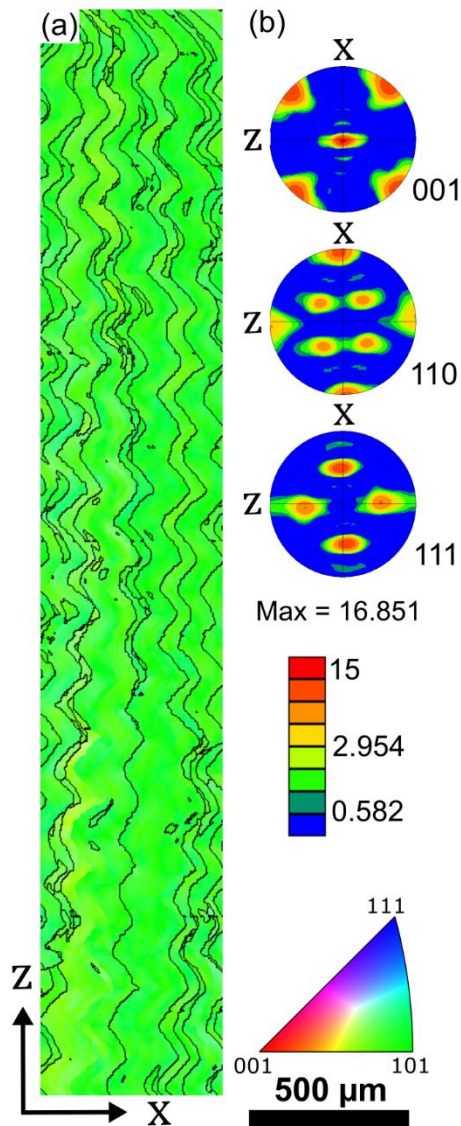


Figure 11. (a) EBSD-IPF map of the microstructure produced using the scanning strategy (3). (b) (001), (110) and (111) Pole figures. Grain boundaries are displayed in black and are associated with interfaces having a misorientation angle $> 15^\circ$.

Some microstructural observations were carried out to validate the schematics shown in **Figure 2 (d)** that reflects the effect of the molten pool geometry and hatch spacing on texture development and grain boundary morphology. An optical micrograph of the topmost layer is shown in **Figure 12 (a)** where the melt pool boundaries and grain boundaries have been revealed by chemical etching and highlighted respectively with green lines and black dotted lines. Note that the scanning direction is systematically perpendicular to the plane of observation of the micrograph shown in **Figure 12 (a)**. The front view of the melt pools is revealed for every single layer because the hatch depth, i.e. the increment of height at which the scanning direction changes, is taken equal to half a layer so that the scanning pattern rotates by 180° at each layer. The comparison of the melt pool shape observed in the topmost layer between the sample fabricated using the scanning strategy (3) and the sample produced with the scanning strategy (1) is given in **Figures 12 (c) and (d)**. The melt pool depth was measured to be about 200-250 μm vs. nearly 70 μm for the scanning strategy (1) resulting in an aspect ratio close to 0.3. The overlap between adjacent tracks is also very large with this scanning strategy as illustrated in **Figures 12 (a) and (c)**. Thus, the bottom of the melt pool, where the thermal gradient is parallel to the build direction, is systematically remelted when melting the adjacent track. **Figure 12 (a)** shows that grains are all tilted in the same direction in each layer (tilted to the right in this case).

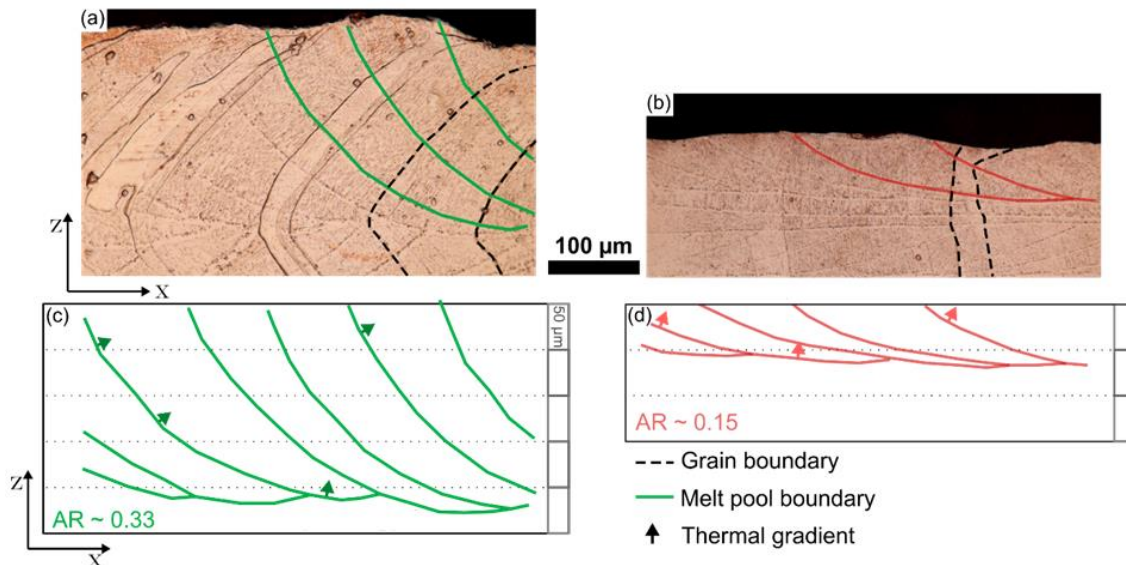


Figure 12 : Optical micrographs of (a) the sample built with the scanning strategy (3) and (b) the sample fabricated using scanning strategy (1) where both the grain and the melt pool boundaries have been revealed by chemical etching. Schematic illustrations of the melt pool shapes of (c) the sample produced using scanning strategy (3) and (d) the sample built using scanning strategy (1). Those illustrations are based on the optical micrographs shown in (a) and (b). The thermal gradient directions, perpendicular to the solid/liquid interface, are indicated with arrows.

To better reveal the link between the molten pools arrangement and the microstructure, an optical micrograph and an EBSD-IPF map taken in the same region of interest are displayed in **Figure 13 (a)** and **Figure 13 (b)** respectively. The melt pool boundaries have been superimposed and highlighted in black. The direction of grain growth changes at every layer, following the change in the direction of the thermal gradient, leading to the formation of wavy columnar grains. Based on the optical microscopy observations, the thermal gradient direction is mainly oriented at nearly 45° relatively to the build direction.

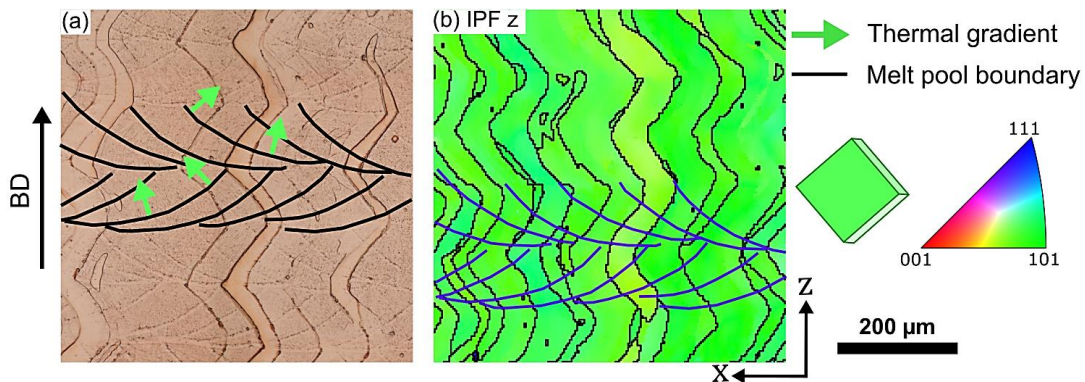


Figure 13: (a) Optical micrograph of the sample built with scanning strategy 4 where the grain and the melt pool boundaries have been revealed by chemical etching. Thirteen melt pool boundaries over two layers are highlighted with black lines, and some selected thermal gradient directions are represented with green arrows. (b) EBSD-IPF-A1 (BD) map of the sample obtained with scanning strategy 4. The melt pool boundaries of the micrographs are superimposed on the EBSD-IPF map.

Since the scanning pattern rotates by 180° at each layer, the thermal gradients between two consecutive layers are roughly perpendicular, as is the direction of grain growth. According to Pham *et al.* [49], in such a situation, a side-branching mechanism between successive layers is promoted. Side-branching is defined as the epitaxial growth between two perpendicular growth directions which is made possible thanks to the symmetry of the cubic unit cell. In such a situation, the change of thermal gradient direction does not stop the epitaxial growth of the $\langle 110 \rangle$ -oriented grains growing over several millimeters as shown in **Figure 11 (a)**.

In summary, the scanning strategy (3) is successful to produce a strong Goss texture but this goes along with a change of grain boundary morphology. This microstructure results from a deep hemispherical melt pool being highly overlapped to promote side-branching. One could imagine keeping the same hatching direction at each layer (no rotation of the hatching direction) to preserve more regular grain boundaries. Such strong Goss textures could also be produced using PBF-LB as reported in [28,61] among others.

5. Conclusion

Through a few illustrative examples, we show that it is possible to tailor the texture of pure copper produced by PBF-EB. The strategy suggested relies on the links between the molten pool morphology and texture development. We show that the melt pool geometry is controlled by the first-order processing parameters (power and scanning speed) as well as by key parameters describing the scanning pattern such as the hatch spacing (line offset) and scanning trajectories. The control of the molten pool geometry and their degree of overlapping is the key to achieving different textures. Large molten pools stretched in the direction perpendicular to the scanning direction with small aspect ratios promote the formation of a Cube texture. On the opposite, promoting the formation of more hemispherical molten pools, typically with aspect ratios larger than 0.3 allows a Goss texture to be produced. The hatch spacing could be further utilized to control the proportion of grains exhibiting a Cube or a Goss texture. We believe that the simple approach proposed in this work and validated on pure copper (a model FCC-metal) could be further used to tailor the texture of other cubic materials such as Al-alloys, Ni-based superalloys, or copper alloys whose properties (yield strength, creep, work-hardening rate) would be more sensitive to the crystallographic texture. This piece of work could also be useful for those interested in validating numerical approaches coupling thermal calculations with cellular automaton to predict the grain structures (size, shape and crystallographic texture) depending on the melting parameters and scanning strategy.

Declaration of competing interest

The authors declare that they have no competing interests.

Acknowledgments

Schneider-Electric is gratefully acknowledged for the financial support of the present study. The authors are grateful to the LERMPS (Laboratoire d'Etudes sur les Matériaux, les Procédés, et les Surfaces) for the production of the powder used in this work. The present study was carried out in the framework of the FUI-Ambition research program. This work has benefited from the characterization equipment of the Grenoble INP - CMTC platform supported by the Centre of Excellence of Multifunctional Architected Materials "CEMAM" n°ANR-10-LABX-44-01 funded by the Investments for the Future program.

References

- [1] L. Liu, B. Yi, T. Wang, Z. Li, J. Zhang, G. Ho, Investigation on numerical analysis and mechanics experiments for topology optimization of functionally graded lattice structure, *Additive Manufacturing*. 47 (2021) 102275. <https://doi.org/10.1016/j.addma.2021.102275>.
- [2] J. Robbins, S.J. Owen, B.W. Clark, T.E. Voth, An efficient and scalable approach for generating topologically optimized cellular structures for additive manufacturing, *Additive Manufacturing*. 12 (2016) 296–304. <https://doi.org/10.1016/j.addma.2016.06.013>.
- [3] A.D. Plessis, I. Yadroitsava, I. Yadroitsev, Effects of defects on mechanical properties in metal additive manufacturing : A review focusing on X-ray tomography insights, *Materials & Design*. 187 (2020) 108385. <https://doi.org/10.1016/j.matdes.2019.108385>.
- [4] S. Romano, A. Abel, J. Gumpinger, A.D. Brandão, S. Beretta, Quality control of AlSi10Mg produced by SLM: metallography versus CT scans for critical defect size assessment, *Additive Manufacturing*. 28 (2019) 394–405. <https://doi.org/10.1016/j.addma.2019.05.017>.
- [5] S. Beretta, S. Romano, A comparison of fatigue strength sensitivity to defects for materials manufactured by AM or traditional processes, *International Journal of Fatigue*. 94 (2017) 178–191. <https://doi.org/10.1016/j.ijfatigue.2016.06.020>.

- [6] T. Debroy, H.L. Wei, J.S. Zuback, T. Mukherjee, J.W. Elmer, J.O. Milewski, A.M. Beese, A. Wilson-heid, A. De, W. Zhang, Progress in Materials Science Additive manufacturing of metallic components – Process , structure and properties, 92 (2018) 112–224. <https://doi.org/10.1016/j.pmatsci.2017.10.001>.
- [7] T. Persenot, G. Martin, R. Dendievel, J.Y. Buffière, E. Maire, Enhancing the tensile properties of EBM as-built thin parts: Effect of HIP and chemical etching, Materials Characterization. 143 (2018) 82–93. <https://doi.org/10.1016/j.matchar.2018.01.035>.
- [8] S. Tammas-Williams, P.J. Withers, I. Todd, P.B. Prangnell, The Influence of Porosity on Fatigue Crack Initiation in Additively Manufactured Titanium Components, Scientific Reports. 7 (2017) 1–13. <https://doi.org/10.1038/s41598-017-06504-5>.
- [9] T. Persenot, J.-Y. Buffiere, E. Maire, R. Dendievel, G. Martin, Fatigue properties of EBM as-built and chemically etched thin parts, Procedia Structural Integrity. 7 (2017) 158–165. <https://doi.org/10.1016/j.prostr.2017.11.073>.
- [10] T. Persenot, A. Burr, E. Plancher, J. Bu, R. Dendievel, G. Martin, Effect of ultrasonic shot peening on the surface defects of thin struts built by electron beam melting : Consequences on fatigue resistance, 28 (2019) 821–830. <https://doi.org/10.1016/j.addma.2019.06.014>.
- [11] B.G. Pyka, A. Burakowski, G. Kerckhofs, M. Moesen, S.V. Bael, J. Schrooten, M. Wevers, Surface Modification of Ti6Al4V Open Porous Structures Produced by Additive Manufacturing, 14 (2012) 363–370. <https://doi.org/10.1002/adem.201100344>.
- [12] P. Lhuissier, C. de Formanoir, G. Martin, R. Dendievel, S. Godet, Geometrical control of lattice structures produced by EBM through chemical etching: Investigations at the scale of individual struts, Materials and Design. 110 (2016) 485–493. <https://doi.org/10.1016/j.matdes.2016.08.029>.
- [13] S. Tammas-williams, P.J. Withers, I. Todd, P.B. Prangnell, The Effectiveness of Hot Isostatic Pressing for Closing Porosity in Selective Electron Beam Melting, Metallurgical and Materials Transactions A. 47 (2016) 1939–1946. <https://doi.org/10.1007/s11661-016-3429-3>.
- [14] B. Attard, S. Cruchley, C. Beetz, M. Megahed, Y.L. Chiu, M.M. Attallah, Microstructural control during laser powder fusion to create graded microstructure Ni-superalloy components, Additive Manufacturing. 36 (2020) 101432. <https://doi.org/10.1016/j.addma.2020.101432>.
- [15] S.P. Narra, R. Cunningham, J. Beuth, A.D. Rollett, Location specific solidification microstructure control in electron beam melting of Ti-6Al-4V, Additive Manufacturing. 19 (2018) 160–166. <https://doi.org/10.1016/j.addma.2017.10.003>.
- [16] P. Köhnen, S. Ewald, J. Henrich, A. Belyakov, C. Haase, Controlling microstructure and mechanical properties of additively manufactured high-strength steels by tailored solidification, Additive Manufacturing. 35 (2020) 101389. <https://doi.org/10.1016/j.addma.2020.101389>.
- [17] ISO/ASTM 5900:2021, Additive manufacturing — General principles — Fundamentals and vocabulary, (2021). <https://www.iso.org/standard/74514.html>.
- [18] H. Helmer, A. Bauereiß, R.F. Singer, C. Körner, Grain structure evolution in Inconel 718 during selective electron beam melting, Materials Science and Engineering A. 668 (2016) 180–187. <https://doi.org/10.1016/j.msea.2016.05.046>.
- [19] E. Chauvet, P. Kontis, E.A. Jägle, B. Gault, D. Raabe, C. Tassin, J.J. Blandin, R. Dendievel, B. Vayre, S. Abed, G. Martin, Hot cracking mechanism affecting a non-weldable Ni-based superalloy produced by selective electron Beam Melting, Acta Materialia. 142 (2018) 82–94. <https://doi.org/10.1016/j.actamat.2017.09.047>.
- [20] R.R. Dehoff, M.M. Kirka, F.A. List, K.A. Unocic, W.J. Sames, Crystallographic texture engineering through novel melt strategies via electron beam melting: Inconel 718, Materials Science and Technology. 31 (2014) 939–944. <https://doi.org/10.1179/1743284714y.0000000697>.
- [21] C.D. Formanoir, S. Michotte, O. Rigo, L. Germain, Electron beam melted Ti – 6Al – 4V : Microstructure , texture and mechanical behavior of the as-built and heat-treated material, Materials Science & Engineering A. 652 (2016) 105–119. <https://doi.org/10.1016/j.msea.2015.11.052>.
- [22] S. Al-Bermani, M. Blackmore, W. Zhang, I. Todd, The Origin of Microstructural Diversity, Texture, and Mechanical Properties in Electron Beam Melted Ti-6Al-4V, Metallurgical and Materials Transactions A: Physical Metallurgy and Materials Science. 41 (2010) 3422–3434. <https://doi.org/10.1007/s11661-010-0397-x>.

- [23] A.A. Antonysamy, J. Meyer, P.B. Prangnell, Effect of build geometry on the β -grain structure and texture in additive manufacture of Ti-6Al-4V by selective electron beam melting, *Materials Characterization*. 84 (2013) 153–168. <https://doi.org/10.1016/j.matchar.2013.07.012>.
- [24] D. Wei, Y. Koizumi, A. Chiba, K. Ueki, K. Ueda, Heterogeneous microstructures and corrosion resistance of biomedical Co-Cr-Mo alloy fabricated by electron beam melting (EBM), *Additive Manufacturing*. 24 (2018) 103–114. <https://doi.org/10.1016/j.addma.2018.09.006>.
- [25] Y. Zhao, Y. Koizumi, K. Aoyagi, D. Wei, K. Yamanaka, Comprehensive study on mechanisms for grain morphology evolution and texture development in powder bed fusion with electron beam of Co-Cr-Mo alloy, *Materialia*. 6 (2019) 100346. <https://doi.org/10.1016/j.mtla.2019.100346>.
- [26] X.Y. He, H. Wang, Z.G. Zhu, L.Z. Wang, J.Q. Liu, N. Haghdadi, S.M.L. Nai, J. Huang, S. Primig, S.P. Ringer, X.Z. Liao, Texture evolution in a CrMnFeCoNi high-entropy alloy manufactured by laser powder bed fusion, *J Mater Sci*. (2022). <https://doi.org/10.1007/s10853-022-07025-x>.
- [27] M. Seleznev, R. Wagner, A. Weidner, M. Wendler, O. Volkova, H. Biermann, Direct tuning of the microstructural and mechanical properties of high-alloy austenitic steel by electron beam melting, *Additive Manufacturing*. 47 (2021) 102253. <https://doi.org/10.1016/j.addma.2021.102253>.
- [28] O. Andreau, I. Koutiri, P. Peyre, J. Penot, N. Saintier, E. Pessard, T. De Terris, C. Dupuy, T. Baudin, Texture control of 316L parts by modulation of the melt pool morphology in selective laser melting, *Journal of Materials Processing Tech*. 264 (2019) 21–31. <https://doi.org/10.1016/j.jmatprotec.2018.08.049>.
- [29] A. Leicht, C.H. Yu, V. Luzin, U. Klement, E. Hryha, Effect of scan rotation on the microstructure development and mechanical properties of 316L parts produced by laser powder bed fusion, *Materials Characterization*. 163 (2020) 110309. <https://doi.org/10.1016/j.matchar.2020.110309>.
- [30] R. Guschlbauer, S. Momeni, F. Osmanlic, C. Körner, Process development of 99.95% pure copper processed via selective electron beam melting and its mechanical and physical properties, *Materials Characterization*. 143 (2018) 163–170. <https://doi.org/10.1016/j.matchar.2018.04.009>.
- [31] Z. Fu, C. Körner, Actual state-of-the-art of electron beam powder bed fusion, *European Journal of Materials*. 2 (2022) 54–117. <https://doi.org/10.1080/26889277.2022.2040342>.
- [32] R.R. Dehoff, M.M. Kirka, W.J. Sames, H. Bilheux, A.S. Tremsin, L.E. Lowe, S.S. Babu, Site specific control of crystallographic grain orientation through electron beam additive manufacturing, *Materials Science and Technology*. 31 (2014) 931–938. <https://doi.org/10.1179/1743284714y.0000000734>.
- [33] N. Raghavan, S. Simunovic, R. Dehoff, A. Plotkowski, J. Turner, M. Kirka, S. Babu, Localized melt-scan strategy for site specific control of grain size and primary dendrite arm spacing in electron beam additive manufacturing, *Acta Materialia*. 140 (2017) 375–387. <https://doi.org/10.1016/j.actamat.2017.08.038>.
- [34] N. Raghavan, R. Dehoff, S. Pannala, S. Simunovic, M. Kirka, J. Turner, N. Carlson, S.S. Babu, Numerical modeling of heat-transfer and the influence of process parameters on tailoring the grain morphology of IN718 in electron beam additive manufacturing, *Acta Materialia*. 112 (2016) 303–314. <https://doi.org/10.1016/j.actamat.2016.03.063>.
- [35] P. Kontis, E. Chauvet, Z. Peng, J. He, A. Kwiatkowski, D. Raabe, C. Tassin, J. Blandin, Atomic-scale grain boundary engineering to overcome hot-cracking in additively-manufactured superalloys, *Acta Materialia*. 177 (2019) 209–221. <https://doi.org/10.1016/j.actamat.2019.07.041>.
- [36] E. Chauvet, C. Tassin, J.J. Blandin, R. Dendievel, G. Martin, Producing Ni-base superalloys single crystal by selective electron beam melting, *Scripta Materialia*. 152 (2018) 15–19. <https://doi.org/10.1016/j.scriptamat.2018.03.041>.
- [37] M. Ramsperger, C. Meid, D. Bu, Microstructure and Mechanical Properties of CMSX-4 Single Crystals Prepared by Additive Manufacturing, *Metallurgical and Materials Transactions A: Physical Metallurgy and Materials Science*. 49 (2018) 3781–3792. <https://doi.org/10.1007/s11661-018-4762-5>.
- [38] P. Fernandez-zelaia, M.M. Kirka, A. Márquez, Y. Lee, S.N. Dryepontd, Nickel-based superalloy single crystals fabricated via electron beam melting, *Acta Materialia*. 216 (2021) 117133. <https://doi.org/10.1016/j.actamat.2021.117133>.

- [39] S.D. Jadhav, S. Dadbakhsh, L. Goossens, J. -p Kruth, J.V. Humbeeck, K. Vanmeensel, Influence of selective laser melting process parameters on texture evolution in pure copper, *Journal of Materials Processing Tech.* 270 (2019) 47–58. <https://doi.org/10.1016/j.jmatprotec.2019.02.022>.
- [40] S.D. Jadhav, L. Rapha, Y. Kinds, B.V. Hooreweder, K. Vanmeensel, Laser-based powder bed fusion additive manufacturing of pure copper, *Additive Manufacturing.* 42 (2021) 101990. <https://doi.org/10.1016/j.addma.2021.101990>.
- [41] X. Yan, C. Chang, D. Dong, S. Gao, W. Ma, M. Liu, H. Liao, S. Yin, Microstructure and mechanical properties of pure copper manufactured by selective laser melting, *Materials Science & Engineering A.* 789 (2020) 139615. <https://doi.org/10.1016/j.msea.2020.139615>.
- [42] N.P. Calta, J. Wang, A.M. Kiss, A.A. Martin, P.J. Depond, G.M. Guss, A.Y. Fong, J.N. Weker, K.H. Stone, C.J. Tassone, J. Matthew, M.F. Toney, A.V. Buuren, M.J. Matthews, N.P. Calta, J. Wang, A.M. Kiss, A.A. Martin, P.J. Depond, G.M. Guss, V. Thampy, A.Y. Fong, J.N. Weker, K.H. Stone, C.J. Tassone, M.J. Kramer, M.F. Toney, A.V. Buuren, M.J. Matthews, An instrument for in situ time-resolved X-ray imaging and diffraction of laser powder bed fusion additive manufacturing processes An instrument for in situ time-resolved X-ray imaging and diffraction of laser powder bed fusion additive manufacturing proce, *Review of Scientific Instruments.* 89 (2018) 055101. <https://doi.org/10.1063/1.5017236>.
- [43] M. Schneider, L. Berthe, R. Fabbro, M. Muller, Measurement of laser absorptivity for operating parameters characteristic of, 2008. 41 (n.d.) 155502. <https://doi.org/10.1088/0022-3727/41/15/155502>.
- [44] R. Guschlbauer, A.K. Burkhardt, Z. Fu, C. Körner, Effect of the oxygen content of the powder on the selective electron beam melting of pure copper, *Materials Science & Engineering A.* (2020) 139106. <https://doi.org/10.1016/j.msea.2020.139106>.
- [45] P. Frigola, O.A. Harrysson, T.J. Horn, H.A. West, R.L. Aman, J.M. Rigsbee, D.A. Ramirez, F. Medina, R.B. Wicker, E. Rodriguez, Fabricating Copper Components, *Advanced Materials & Processes.* (2014) 20.
- [46] M.A. Lodes, R. Guschlbauer, C. Körner, Process development for the manufacturing of 99.94% pure copper via selective electron beam melting, *Materials Letters.* 143 (2015) 298–301. <https://doi.org/10.1016/j.matlet.2014.12.105>.
- [47] S.J. Raab, R. Guschlbauer, M.A. Lodes, C. Körner, Thermal and Electrical Conductivity of 99.9% Pure Copper Processed via Selective Electron Beam Melting, *Advanced Engineering Materials.* 18 (2016) 1661–1666. <https://doi.org/10.1002/adem.201600078>.
- [48] A. Thomas, G. Fribourg, J. Blandin, P. Lhuissier, R. Dendievel, G. Martin, Effect of the build orientation on mechanical and electrical properties of pure Cu fabricated by E-PBF, *Additive Manufacturing.* 48 (2021) 102393. <https://doi.org/10.1016/j.addma.2021.102393>.
- [49] M.-S. Pham, B. Dovggy, P.A. Hooper, C.M. Gourlay, A. Piglione, The role of side-branching in microstructure development in laser powder-bed fusion, *Nature Communications.* 749 (2020) 1–12. <https://doi.org/10.1038/s41467-020-14453-3>.
- [50] M. Galati, L. Iuliano, A literature review of powder-based electron beam melting focusing on numerical simulations, *Additive Manufacturing.* 19 (2018) 1–20. <https://doi.org/10.1016/j.addma.2017.11.001>.
- [51] Y. Zhao, Y. Koizumi, K. Aoyagi, D. Wei, K. Yamanaka, Comprehensive study on mechanisms for grain morphology evolution and texture development in powder bed fusion with electron beam of Co – Cr – Mo alloy, *Materialia.* 6 (2019) 100346. <https://doi.org/10.1016/j.mtla.2019.100346>.
- [52] A. Plotkowski, M.M. Kirka, S.S. Babu, Verification and validation of a rapid heat transfer calculation methodology for transient melt pool solidification conditions in powder bed metal additive manufacturing, *Additive Manufacturing.* 18 (2017) 256–268. <https://doi.org/10.1016/j.addma.2017.10.017>.
- [53] A. Plotkowski, M.M. Kirka, S.S. Babu, Verification and validation of a rapid heat transfer calculation methodology for transient melt pool solidification conditions in powder bed metal additive manufacturing, *Additive Manufacturing.* 18 (2017) 256–268. <https://doi.org/10.1016/j.addma.2017.10.017>.
- [54] C. Breuning, C. Arnold, M. Markl, K. Carolin, A multivariate melt pool stability criterion for fabrication of complex geometries in electron beam powder bed fusion, *Additive Manufacturing.* 45 (2021) 102051. <https://doi.org/10.1016/j.addma.2021.102051>.

- [55] P. Promopattum, S.-C. Yao, P.C. Pistorius, A.D. Rollett, A Comprehensive Comparison of the Analytical and Numerical Prediction of the Thermal History and Solidification Microstructure of Inconel 718 Products Made by Laser Powder-Bed Fusion, *Engineering*. 3 (2017) 685–694. <https://doi.org/10.1016/J.ENG.2017.05.023>.
- [56] P. Frigola, O.A. Harrysson, T.J. Horn, H.A. West, R.L. Aman, J.M. Rigsbee, D.A. Ramirez, F. Medina, R.B. Wicker, E. Rodriguez, Fabricating Copper Components with Electron Beam Melting, *Advanced Materials & Processes*. (2014) 20–24.
- [57] B. Bacroix, S. Queyreau, D. Chaubet, E. Siv, T. Chauveau, The influence of the cube component on the mechanical behaviour of copper polycrystalline samples in tension, *Acta Materialia*. 160 (2018) 121–136. <https://doi.org/10.1016/j.actamat.2018.08.044>.
- [58] M. Ramsperger, C. Meid, D. Bu, Microstructure and Mechanical Properties of CMSX-4 Single Crystals Prepared by Additive Manufacturing, *Metallurgical and Materials Transactions A: Physical Metallurgy and Materials Science*. 49 (2018) 3781–3792. <https://doi.org/10.1007/s11661-018-4762-5>.
- [59] E. Chauvet, C. Tassin, J.J. Blandin, R. Dendievel, G. Martin, Producing Ni-base superalloys single crystal by selective electron beam melting, *Scripta Materialia*. 152 (2018) 15–19. <https://doi.org/10.1016/j.scriptamat.2018.03.041>.
- [60] K.A. Sofinowski, S. Raman, X. Wang, B. Gaskey, M. Seita, Layer-wise engineering of grain orientation (LEGO) in laser powder bed fusion of stainless steel 316L, *Additive Manufacturing*. 38 (2021) 101809. <https://doi.org/10.1016/j.addma.2020.101809>.
- [61] M.-S. Pham, B. Dovgyy, P.A. Hooper, C.M. Gourlay, A. Piglione, The role of side-branching in microstructure development in laser powder-bed fusion, *Nature Communications*. 749 (2020) 1–12. <https://doi.org/10.1038/s41467-020-14453-3>.